Materials Advances

ROYAL SOCIETY OF CHEMISTRY

PAPER

View Article Online
View Journal | View Issue

Cite this: *Mater. Adv.*, 2025, 6, 3185

Bioactive hyperbranched polymer dot combined laser-induced optical breakdown for accelerating wound repair and regeneration in a nude mice model†

Chang-Cheng Chang,[abc] Hoi-Man Iao,[c] Siao-Cian Fan,[c] Yi-Hsuan Tu,[b] Jia-Chee Siew,[b] Kang-Chiao Ma,[c] Yu-Hsuan Lee,[c] Hsiu-Mei Chiang,[c] Ching-Chang Cheng[d] and Tzong-Yuan Juang *[c]

Chronic wounds pose a significant challenge in clinical practice, with current treatments often failing to address the complex underlying pathophysiology. This study introduces a novel therapeutic strategy combining bioactive hyperbranched polymer dots (PDs) with picosecond laser-induced optical breakdown (LIOB) to synergistically enhance wound healing. The bioactive PDs exhibited unique antioxidant activity, decreasing the degree of oxidative stress, and featured wholly-aliphatic hyperbranched poly(amic acid) structures with low cytotoxicity and nanoscale dimensions of approximately 10 nm in aqueous environments. In a nude mouse model, the PDs + LIOB combination therapy significantly accelerated wound closure, with a 75.13% reduction in wound size by day 6 compared to untreated controls. Histological and molecular analyses revealed enhanced angiogenesis, stem cell recruitment, and collagen deposition in the PDs + LIOB group, as evidenced by increased expression of CD31 and CD34, and a higher type I/III collagen ratio. Optical coherence tomography confirmed the formation of persistent cavitation bubbles at the dermal–epidermal junction following LIOB, potentially providing dermal and epidermal repair. Immunohistochemical analysis demonstrated reduced inflammation and MMP-9 expression in the PDs + LIOB group, while ELISA results showed increased levels of TGF-β and Smad2/3, key regulators of wound repair. Masson's trichrome staining revealed more organized and densely packed collagen fibers in the PDs + LIOB group, indicating superior tissue remodeling and reduced fibrosis. This innovative approach harnessed the synergistic effects of LIOB and PDs, with PDs modulating key signaling pathways to accelerate healing and LIOB enhancing the repair functions of dermal and epidermal regeneration. The combination therapy not only accelerated wound closure but also improved scar appearance and tissue regeneration, highlighting its potential as a targeted treatment for chronic wounds. These findings advance the field of wound care, offering a promising solution to address the limitations of current therapies and improve patient outcomes.

Received 17th December 2024,
Accepted 30th March 2025

DOI: 10.1039/d4ma01256a

rsc.li/materials-advances

Introduction

Chronic wounds pose a significant global healthcare challenge, affecting approximately 40 million patients annually and imposing substantial economic burdens exceeding $50 billion on healthcare systems worldwide.[1,2] These wounds are characterized by prolonged healing times, persistent inflammation, and increased susceptibility to infections, often proving resistant to conventional treatment approaches.[2] The wound healing process encompasses a complex and dynamic interplay of overlapping phases: hemostasis, inflammation, proliferation, and remodeling. Central to these processes, transforming growth factor-beta (TGF-β) functions as a pivotal regulator, mediating inflammation resolution, angiogenesis, and collagen synthesis through both small mothers against decapentaplegic (Smad)-dependent and Smad-independent pathways.[3] Dysregulation of TGF-β signaling has been linked to delayed healing and excessive fibrosis, while the mitogen-activated

[a] *Aesthetic Medical Center, China Medical University Hospital, Taichung, Taiwan*
[b] *School of Medicine, China Medical University, Taichung, Taiwan*
[c] *Department of Cosmeceutics, China Medical University, Taichung, Taiwan. E-mail: tyjuang@mail.cmu.edu.tw; Tel: +886-4-22053366-5312*
[d] *Director of Laboratory Animal Service Center, Office of Research and Development, China Medical University, Taichung, Taiwan*

† Electronic supplementary information (ESI) available. See DOI: https://doi.org/10.1039/d4ma01256a

protein kinase (MAPK) pathway critically influences extracellular matrix (ECM) remodeling through its regulation of matrix metalloproteinases (MMPs) and their inhibitors.[4,5] Conventional wound therapies often fail to effectively modulate these pathways, resulting in suboptimal healing outcomes.[6]

The pathophysiology of chronic wounds is fundamentally driven by persistent oxidative stress, which contributes to a self-perpetuating cycle of inflammation and tissue damage.[7–9] This oxidative microenvironment is characterized by elevated levels of reactive oxygen species (ROS), particularly superoxide anions ($^{\bullet}O_2^-$) and hydroxyl radicals ($^{\bullet}OH$), which can overwhelm the endogenous antioxidant defense mechanisms of cells within the wound bed.[8,10] The excessive ROS production not only causes direct cellular damage through lipid peroxidation and protein carbonylation but also impairs critical wound healing processes by disrupting cell signaling pathways, inhibiting fibroblast proliferation, and degrading ECM components.[11] Consequently, interventions targeting oxidative stress have emerged as promising strategies for breaking this pathological cycle and promoting wound repair.

Recent advances in carbon nanodots have led to the development of hyperbranched polymer dots (PDs) with nanocluster sizes below 10 nm as promising therapeutic agents for wound healing applications.[12] These carbon nanodots exhibit unique physicochemical properties, including superior water solubility, targeted tissue distribution,[13] and enhanced skin epithelial–mesenchymal transition (EMT) characteristics.[14] Carbon-based nanomaterials possess inherent antioxidant properties due to their high electron affinity, allowing them to efficiently scavenge ROS such as $^{\bullet}O_2^-$ and $^{\bullet}OH$ through mechanisms similar to the grafting of organic functional groups.[15] The presence of oxygen-containing functional groups (hydroxyl, aldehyde, carboxyl, and ketone) on the carbon nanodot surface enables them to act as proton donors and transfer free electrons to neutralize harmful radicals.[16] Furthermore, these nanomaterials can modulate cellular antioxidant responses by enhancing nuclear factor erythroid 2-related factor 2 (Nrf2) signaling, upregulating phase II antioxidant enzymes, and ultimately reducing oxidative stress-induced apoptosis.[17]

Our previous studies demonstrated that hyperbranched PDs, synthesized through an $A_2 + B_3$ polymerization strategy, possess exceptional biocompatibility and cellular uptake efficiency.[18–20] Our recent findings revealed that PDs exhibit both antibacterial[18] and antioxidant activities by effectively scavenging free radicals,[20] contributing to a significant reduction in oxidative stress for skin repair. Beyond their direct ROS-scavenging capabilities, carbon nanodots can activate the TGF-β non-Smad pathway, specifically the p38 MAPK/Snail signaling axis, to induce EMT.[21] This process upregulates EMT markers such as fibronectin and vimentin, promoting cell migration and accelerating re-epithelialization at the wound edge.[22] The enhanced epithelial cell migration facilitates rapid barrier formation, which limits external stimuli, reduces inflammatory responses, and regulates granulation tissue formation and collagen deposition. These properties, combined with their ability to modulate key molecular pathways, position PDs as ideal candidates for advanced wound healing therapies.

Picosecond laser-induced optical breakdown (LIOB) technology has emerged as a sophisticated approach for repair functions of dermal and epidermal regeneration.[23] By utilizing ultrafast laser pulses, a picosecond laser creates precisely controlled microchannels in tissue, facilitating LIOB-mediated dermal and epidermal regeneration while minimizing collateral thermal damage. The picosecond laser generates cavitation effects and shockwave propagation within the dermis without disrupting the epidermal layer, delivering ultrafast oscillatory energy that penetrates the deeper collagen-rich regions.[24] This process leads to controlled collagen fragmentation and activation of wound repair signaling pathways, particularly through the TGF-β/Smad axis.[25] Recent studies have demonstrated LIOB's capacity to modulate wound healing pathways, particularly the TGF-β/Smad and p38 MAPK cascades, through controlled mechanical tissue disruption and subsequent regenerative responses.[23] The mechanical stimulation induced by LIOB activates mechanosensitive pathways, including the Yes-associated protein/transcriptional coactivator with the PDZ-binding motif (YAP/TAZ) pathway, which plays a crucial role in cellular mechanotransduction and tissue repair.[26,27] These mechanotransduction signals synergize with growth factor-mediated pathways to enhance fibroblast activation, myofibroblast differentiation, and ECM remodeling.[27,28] These findings suggest that LIOB could serve as an ideal complementary technology for enhancing PD-based therapeutic strategies.

Despite these promising advances in both PD development and LIOB technology, their potential synergistic effects in wound healing applications remain unexplored. This knowledge gap is particularly significant given the complex nature of chronic wound pathophysiology and the limitations of current monotherapeutic approaches. The therapeutic approaches targeting either oxidative stress or mechanical tissue remodeling alone may not adequately address the multifaceted pathology of chronic wounds. We hypothesize that the integration of LIOB with PDs can enhance wound healing outcomes through three distinct mechanisms: (1) bioactive PDs exhibited distinctive antioxidant properties, effectively reducing oxidative stress levels, (2) LIOB enhanced the repair functions of dermal and epidermal regeneration, and (3) PD enhanced the modulation of key signaling pathways.

The molecular synergy between LIOB and PDs likely occurs at multiple levels. LIOB creates microchannels that enhance PD penetration into the wound bed, improving bioavailability and therapeutic efficacy.[29] Additionally, the LIOB-induced mechanical stimulation may promote cellular internalization of PDs through mechanically activated endocytosis pathways.[30] The controlled tissue disruption generated by LIOB also triggers a localized inflammatory response that can be modulated by the anti-inflammatory and antioxidant properties of PDs, preventing excessive inflammation while maintaining the beneficial aspects of the wound healing cascade.[24,31] Furthermore, LIOB and PDs target complementary but distinct molecular

pathways: LIOB primarily acts through the TGF-β/Smad-dependent pathway to promote controlled collagen synthesis and tissue remodeling, while PDs function through the non-Smad p38 MAPK/Snail axis to enhance cell migration and re-epithelialization. This dual pathway activation potentially creates a synergistic effect that comprehensively addresses the multifaceted nature of chronic wounds.

For preclinical evaluation of wound healing therapies, the nude mouse model offers significant advantages that align with our research objectives. The athymic nude mouse model has been extensively validated for wound healing studies due to its epidermal structure and wound healing kinetics that closely resemble human cutaneous wound repair.[32–34] Specifically, nude mice exhibit re-epithelialization patterns, inflammatory responses, and extracellular matrix deposition similar to human wound healing, albeit with reduced contraction compared to wild-type mice.[32,35] This reduced contraction allows for better evaluation of re-epithelialization and granulation tissue formation, which are critical parameters in human wound healing.[32,34] Additionally, the immunocompromised nature of nude mice allows for the study of wound healing processes with minimal interference from adaptive immune responses, providing a clearer assessment of the direct effects of therapeutic interventions on wound repair mechanisms.[32,36] Moreover, this model facilitates future translational research involving human stem cell transplantation, enabling evaluation of cellular therapies in combination with PD-LIOB treatment.[37] These characteristics make the nude mouse model particularly suitable for investigating novel wound healing strategies with potential clinical applications.

The present study investigates our hypothesis through comprehensive analysis of wound healing outcomes following combined PD-LIOB treatment. Specifically, we examine the effects on collagen deposition, inflammatory mediator profiles, and the activation patterns of critical signaling cascades. This investigation represents a significant advancement in regenerative medicine, offering a novel therapeutic paradigm that addresses multiple aspects of the wound healing process while enabling personalized treatment optimization. The development of this PD-LIOB combination therapy has substantial clinical implications, as it could potentially overcome treatment resistance in chronic wounds through its multi-targeted approach. Chronic wounds, particularly those associated with diabetes, pressure, or venous insufficiency, often fail to respond to conventional treatments due to their complex pathophysiology involving persistent inflammation, excessive oxidative stress, and dysregulated tissue remodeling.[7,38] Our approach simultaneously addresses these challenges through the antioxidant properties of PDs and the controlled tissue remodeling effects of LIOB, potentially offering a solution for patients with recalcitrant wounds. Furthermore, this therapy could be personalized based on wound type and patient-specific factors, optimizing treatment parameters to achieve optimal outcomes across diverse clinical scenarios. The findings from this study may establish a new standard for chronic wound management, potentially overcoming the limitations that have historically challenged conventional therapeutic strategies and improving quality of life for millions of patients worldwide.

Materials and methods

Hyperbranched polymer dot (PD) synthesis

The hyperbranched polymer dots (PDs) used in this study were synthesized using an A_2 + B_3 polymerization strategy as previously described.[19] Briefly, two types of dianhydrides, bicyclo[2.2.2]oct-7-ene-2,3,5,6-tetracarboxylic dianhydride (BCDA) and ethylenediaminetetraacetic dianhydride (EDTAD), were used as the A_2 components, while Jeffamine T403 polyetheramine was employed as the B_3 component. The resulting PDs, named PD-BT (from BCDA) and PD-ET (from EDTAD), possessed hyperbranched poly(amic acid) structures with terminal amino groups. For this study, PD-ET was selected due to its favorable properties, including high water solubility, strong fluorescence, and low cytotoxicity.[19]

Structural and physicochemical characterization of the PDs

The chemical structure of the PDs was confirmed using Fourier transform infrared spectroscopy (FTIR) (Nicolet iS5, Thermo Fisher Scientific, USA) in the range of 4000–400 cm^{-1}. Nuclear magnetic resonance (NMR) spectroscopy (Bruker Avance III 500 MHz, Germany) was employed to further verify the structure, with samples dissolved in DMSO-d_6. The optical properties of PDs were characterized using UV-visible spectrophotometry (UV-2600, Shimadzu, Japan) in the range of 200–800 nm and fluorescence spectroscopy (F-7000, Hitachi, Japan) with excitation at 360 nm and emission measured from 380 to 600 nm. The fluorescence quantum yield was determined using quinine sulfate in 0.1 M H_2SO_4 (quantum yield = 0.54) as a reference standard. The zeta potential of PDs was measured using a Zetasizer Nano ZS90 (Malvern Instruments, UK) at 25 °C with a scattering angle of 90°. Samples were prepared at a concentration of 0.1 mg mL^{-1} in deionized water and measurements were performed in triplicate.

PD hydrogel formulation

Polyethylene glycol 1000 (PEG1000) (Alfa Aesar, USA) was used as a thickening agent to prepare the PD hydrogel formulation. PEG1000 is a biocompatible and water-soluble polymer widely used in pharmaceutical and biomedical applications.[39] The PD hydrogel was prepared by dissolving PDs (5 mg mL^{-1}) in a 5% PEG1000 solution. The particle sizes and size distribution (polydispersity index, PDI) of the PDs in the hydrogel formulation were determined using a dynamic light scattering (DLS) analyzer (Zetasizer Nano ZS90, Malvern). Measurements were performed at 25 °C with a detection angle of 90°, and each sample was measured in triplicate to ensure reproducibility.

Antioxidant activity of the PDs

Hydroxyl radical scavenging activity assay. The hydroxyl radical scavenging activity of the PDs was evaluated based on a previous report.[40] A stock solution of PDs (300 mg mL^{-1}) was prepared and subsequently diluted to concentrations of 0, 0.1,

0.3, 0.6 and 1.5 mg mL^{-1} to determine dose-dependent effects. The reaction mixtures consisted of $FeCl_3$ (0.1 mM), H_2O_2 (1 mM), KH_2PO_4–KOH buffer (pH 7.4, 20 mM), ascorbic acid (0.1 mM), deoxyribose (2.8 mM), and ethylenediaminetetraacetic acid (EDTA) (0.1 mM), which were combined with the PD solutions and incubated at 37 °C for 40 minutes. Following the addition of thiobarbituric acid (TBA) (1% w/v) and trichloroacetic acid (TCA) (2.8% w/v), the mixtures were further incubated at 100 °C for 15 minutes. After cooling, the samples were centrifuged at 3000 rpm for 10 minutes to separate the supernatant, which was analyzed for absorbance at 532 nm using a microplate reader (SpectraMax M5, Molecular Devices, USA). Mannitol (10 mM) was used as a positive control, and the scavenging activity was calculated using the following equation:

$$\text{Scavenging activity (\%)} = [(A_0 - A_1)/A_0] \times 100$$

where A_0 is the absorbance of the control (without PDs) and A_1 is the absorbance in the presence of PDs or the positive control.

Superoxide anion radical scavenging activity assay. PD solutions (300 mg mL^{-1}) were diluted to concentrations of 0, 0.1, 0.3, 0.6, and 1.5 mg mL^{-1} and mixed with phenazine methosulfate (PMS) (10 μM), dihydronicotinamide adenine dinucleotide (NADH) (78 μM), and nitroblue tetrazolium (NBT) (25 μM) in phosphate buffer (pH 7.4, 0.1 M). The mixtures were allowed to react at room temperature for 5 minutes. The absorbance of the resulting solutions was measured at 570 nm using a microplate reader. Butylated hydroxytoluene (BHT) (250 μg mL^{-1}) was used as a positive control, and the scavenging activity was calculated using the same equation as for hydroxyl radical scavenging. These assays provide quantitative measures of the antioxidant efficacy of PDs in scavenging free radicals, which is crucial for understanding their potential in mitigating oxidative stress in wound environments.

Animal model and ethical approval

BALB/cAnN.Cg-Foxn1nu/CrlNarl nude mice (8-week-old, female) were purchased from the National Laboratory Animal Center (Taipei, Taiwan). All animal experiments were approved by the Institutional Animal Care and Use Committee of China Medical University (protocol no. CMUIACUC-2021-118). The nude mouse model was selected for this study based on its established validity for wound healing research.[36,41] This model offers several advantages, including an epidermal structure and wound healing kinetics that closely mimic human cutaneous wound repair, reduced wound contraction compared to wild-type mice (allowing better evaluation of re-epithelialization), and the ability to clearly assess the direct effects of therapeutic interventions with minimal interference from adaptive immune responses. Animals were housed in a controlled environment (12-hour light/dark cycle, 22 ± 2 °C, 50 ± 10% humidity) with free access to food and water.

Picosecond laser treatment

A 755 nm picosecond laser with a diffractive lens array (PicoSure®, Cynosure, Westford, MA, USA) was used to generate laser-induced optical breakdown (LIOB) in the skin. The laser parameters were optimized based on previous studies[42] and preliminary experiments to achieve effective LIOB while minimizing collateral thermal damage. The parameters were set as follows: spot size, 6 mm (to ensure adequate coverage of the wound area); fluence, 0.71 J cm^{-2} (selected to generate sufficient LIOB without causing excessive tissue damage); pulse duration, 750 ps (ultrashort pulses to minimize thermal effects); and frequency, 5 Hz. For the Laser and Laser + PD groups, 500 pulses were applied to the wound area immediately after wounding. This pulse number was determined through preliminary experiments to achieve optimal tissue disruption and cavitation bubble formation, as visualized by optical coherence tomography.

Optical coherence tomography (OCT)

An optical coherence tomography system (OPXION Technology Inc., Taiwan) with an axial resolution of 8 μm and transverse resolution of 15 μm was employed to non-invasively visualize and monitor the skin morphology and LIOB effects in real-time. OCT imaging was performed before laser treatment, immediately after treatment, and on day 3 post-treatment to assess the formation and persistence of microscopic cavitation bubbles in the skin. Images were acquired at a scan rate of 50 kHz over a scan area of 5 × 5 mm, with an imaging depth of approximately 2 mm. The OCT system utilized a center wavelength of 1310 nm with a bandwidth of 100 nm. Images were processed using manufacturer's software (OPXION Analysis Suite v3.2) to enhance visualization of dermal structures and LIOB-induced changes.

Experimental design and procedures

Mice were randomly divided into five groups (n = 6 per group) using a computer-generated randomization sequence: (1) Control (untreated), (2) PEG1000 (vehicle control), (3) PDs, (4) Laser, and (5) Laser + PDs, as summarized in Fig. S1 (ESI†) for experimental design and procedures. The sample size was determined based on power analysis of preliminary data, with α = 0.05 and power = 0.8. All mice were anesthetized with isoflurane (3% for induction and 1.5% for maintenance) delivered in oxygen at 1 L min^{-1} using a precision vaporizer. After shaving the dorsal fur and disinfecting with 70% ethanol, two full-thickness excisional wounds (6 mm in diameter) were created on the dorsal skin using a sterile biopsy punch (Kai Medical, Japan). To prevent wound contraction and ensure healing primarily through re-epithelialization (similar to human wound healing), silicone splints (inner diameter: 10 mm, outer diameter: 18 mm, and thickness: 0.5 mm) were fixed around the wounds using 6-0 nylon sutures (Ethicon, USA) and medical-grade adhesives (3 M Vetbond, USA).[43]

In the Laser and Laser + PD groups, the wounds were treated with the picosecond laser (500 pulses) immediately after wounding. In the PDs and Laser + PD groups, 200 μL of the PD hydrogel (5 mg mL^{-1} PDs in 5% PEG1000) was topically applied to the wounds every three days (on days 0, 3, 6, 9, 12, and 15). The Control and PEG1000 groups received no treatment or vehicle (5% PEG1000) application, respectively. Wound

healing progress was monitored by capturing digital images of the wounds using a standardized photography setup (constant distance, lighting, and camera settings) on days 0, 3, 6, 9, 12, 15, and 18. A ruler was included in each image for scale calibration. The wound size was measured using ImageJ software (NIH, USA, version 1.53a) by two independent, blinded investigators. The wound area was traced manually along the wound edges, and the software calculated the area in square millimeters. The percentage of wound closure was calculated using the following formula:

$$\text{Wound closure (\%)} = [(A_0 - A_t)/A_0] \times 100$$

where A_0 is the initial wound area (day 0) and A_t is the wound area at time t.

On days 3, 6, and 18 post-wounding, mice ($n = 2$ per group at each time point) were euthanized by CO_2 inhalation followed by cervical dislocation, and wound tissues were harvested for histological and molecular analyses. Each wound was excised with a 2 mm margin of the surrounding healthy tissue. The tissue samples were divided into two portions: one for histological analysis (fixed in 10% neutral buffered formalin) and one for molecular analysis (immediately snap-frozen in liquid nitrogen and stored at −80 °C).

Tissue processing and histological analysis

Tissue samples were fixed in 10% neutral buffered formalin for 24 hours, dehydrated through a graded ethanol series (70%, 80%, 90%, 95%, and 100%, 2 hours each), cleared in xylene (twice, 1 hour each), and embedded in paraffin. Sections (5 μm thick) were cut using a rotary microtome (Leica RM2255, Germany) and mounted on poly-L-lysine-coated glass slides for further analysis.

Immunohistochemistry (IHC)

Immunohistochemical staining was performed to evaluate the expression of key proteins involved in wound healing, including CD31 (angiogenesis marker), CD34 (stem cell marker), and matrix metalloproteinase-9 (MMP-9, involved in extracellular matrix remodeling). Paraffin-embedded tissue sections were deparaffinized in xylene, rehydrated through graded ethanol solutions (100%, 95%, 80%, and 70%), and subjected to heat-induced epitope retrieval in citrate buffer (pH 6.0) using a pressure cooker (20 minutes). Endogenous peroxidase activity was quenched with 3% hydrogen peroxide in methanol for 15 minutes at room temperature. Non-specific binding was blocked using 5% bovine serum albumin (BSA) in PBS for 1 hour. Sections were then incubated with primary antibodies at 4 °C overnight. The following primary antibodies were used: anti-CD31 (ab28364, Abcam, UK, 1 : 100 dilution), anti-CD34 (ab81289, Abcam, UK, 1 : 200 dilution), anti-MMP-9 (ab38898, Abcam, UK, 1 : 100 dilution), anti-p38 MAPK (ab170099, Abcam, UK, 1 : 100 dilution), and anti-fibronectin (ab2413, Abcam, UK, 1 : 200 dilution). After washing with PBS (three times, 5 minutes each), sections were incubated with biotinylated secondary antibodies (Thermo Fisher Scientific, USA, 1 : 500 dilution) for 1 hour at room temperature, followed by streptavidin–HRP (ThermoFisher Scientific, USA) for 30 minutes. The staining was visualized using a 3,3′-diaminobenzidine (DAB) substrate kit (Vector Laboratories, USA) and counterstained with hematoxylin. Negative controls were processed similarly but with the omission of primary antibodies.

Quantitative analysis of IHC staining was performed using ImageJ software. For each marker, five random high-power fields (400×) per section were captured using a light microscope equipped with a digital camera (Olympus BX51, Japan). The images were analyzed using color deconvolution to separate DAB staining from hematoxylin. The area percentage of positive staining was calculated as the ratio of the DAB-positive area to the total tissue area, expressed as a percentage. For CD31, the number of positively stained blood vessels was counted manually in five random fields per section. All analyses were performed by two independent, blinded investigators.

Masson's trichrome staining

Masson's trichrome staining was conducted to assess collagen deposition and tissue remodeling in the wound area. Paraffin-embedded tissue sections were stained using a Masson's trichrome staining kit (ab150686, Abcam, UK) according to the manufacturer's protocol. This staining differentiated between cellular elements (red) and collagen fibers (blue). Briefly, slides were deparaffinized, rehydrated, and fixed in Bouin's solution for 1 hour at 56 °C. After washing in running tap water, sections were stained with Weigert's iron hematoxylin for 10 minutes, followed by Biebrich scarlet-acid fuchsin solution for 10–15 minutes. After differentiation in phosphomolybdic–phosphotungstic acid solution for 10–15 minutes, sections were stained with aniline blue solution for 5–10 minutes, differentiated in 1% acetic acid for 2–5 minutes, dehydrated, cleared, and mounted.

Quantitative analysis of collagen deposition was performed using ImageJ software. Images were captured using a light microscope at 200× magnification, with five random fields per section. The images were split into RGB channels, and the blue channel was used to quantify collagen deposition. The collagen density was calculated as the percentage of blue-stained area relative to the total tissue area. Additionally, collagen fiber organization was assessed using a semi-quantitative scoring system (1 = disorganized thin fibers; 2 = moderately organized fibers; 3 = well-organized thick fibers) by two independent, blinded investigators.

Enzyme-linked immunosorbent assay (ELISA)

For ELISA, frozen tissue samples were homogenized in ice-cold PBS containing protease inhibitors (cOmplete™, Roche, Switzerland) and phosphatase inhibitors (PhosSTOP™, Roche, Switzerland) using a tissue homogenizer (Polytron PT 1200E, Kinematica, Switzerland). Homogenates were centrifuged at 10 000 × g for 15 minutes at 4 °C, and the supernatants were collected. Protein concentrations were determined using a BCA assay kit (ThermoFisher Scientific, USA) with bovine serum albumin as the standard. The protein expression levels of transforming growth factor-beta (TGF-β), Smad2/3, and type I

and III collagen in wound tissues were quantified using ELISA kits (MyBioSource, USA) according to the manufacturer's instructions. Briefly, 100 μL of standards or samples were added to the pre-coated wells and incubated for 2 hours at 37 °C. After washing, biotin-conjugated detection antibodies were added and incubated for 1 hour at 37 °C. Following washing, streptavidin–HRP was added for 30 minutes at 37 °C. After a final wash, TMB substrate was added, and the reaction was stopped with stop solution. The absorbance was measured at 450 nm using a microplate reader. The concentrations of the target proteins were calculated based on the standard curves and normalized to the total protein content. Each sample was analyzed in triplicate to ensure reliability.

Statistical analysis

Data are presented as mean ± standard deviation (SD). Statistical analyses were performed using GraphPad Prism software (version 9.0, GraphPad Software Inc., USA). The normality of data distribution was assessed using the Shapiro–Wilk test. For normally distributed data, one-way or two-way analysis of variance (ANOVA) with Tukey's *post hoc* test was used to compare differences among groups. For non-normally distributed data, the Kruskal–Wallis test followed by Dunn's *post hoc* test was employed. Wound closure over time was analyzed using two-way repeated measures ANOVA followed by Bonferroni's *post hoc* test. The difference in sample size between the Control group (n = 5) and other groups (n = 6) for the ELISA experiments was due to the loss of one animal in the Control group during the study period. This loss was unrelated to the experimental procedures, and statistical analyses were adjusted accordingly to account for the unequal sample sizes. A p-value of < 0.05 was considered statistically significant. To ensure reproducibility, key experiments were performed at least three times independently.

Results

Physical properties and antioxidant activity of PDs

Our PDs were obtained through one-pot condensation polymerizations with wholly-aliphatic hyperbranched poly(amic acid) structures as shown in Fig. 1a. FTIR spectroscopy confirmed the successful synthesis of PDs, with characteristic absorption bands at 3310 cm^{-1} (N–H stretching), 1720 cm^{-1} (C═O stretching of carboxylic acid), 1650 cm^{-1} (C═O stretching of amide), and 1540 cm^{-1} (N–H bending). ^1H NMR spectra further validated the chemical structure, showing signals at δ 8.2–8.6 ppm (NH), δ 3.2–3.6 ppm (CH_2 adjacent to NH), and δ 1.2–1.8 ppm (aliphatic protons). The resulting PDs dispersed well in water, exhibiting a yellow coloration attributed to multi-hydrogen bonding and their zwitterionic globular structure. UV-vis absorption spectroscopy revealed distinct absorption peaks in the range of 220–380 nm, while fluorescence spectroscopy demonstrated strong blue fluorescence with an emission maximum at 438 nm when excited at 360 nm. The fluorescence quantum yield was determined to be 14.0%, indicating efficient fluorescence emission suitable for potential bioimaging applications.

Zeta potential measurements revealed a value of −23.4 ± 2.7 mV, suggesting good colloidal stability in aqueous environments. Dynamic light scattering (DLS) analysis indicated that the PD hydrogel, designed for animal wound therapy and prepared with a concentration of 5 mg mL^{-1} PDs in a 5% PEG1000 aqueous solution, had an average particle diameter of 10.4 ± 1.2 nm with a polydispersity index (PDI) of 0.32 ± 0.04 (Fig. 1b).

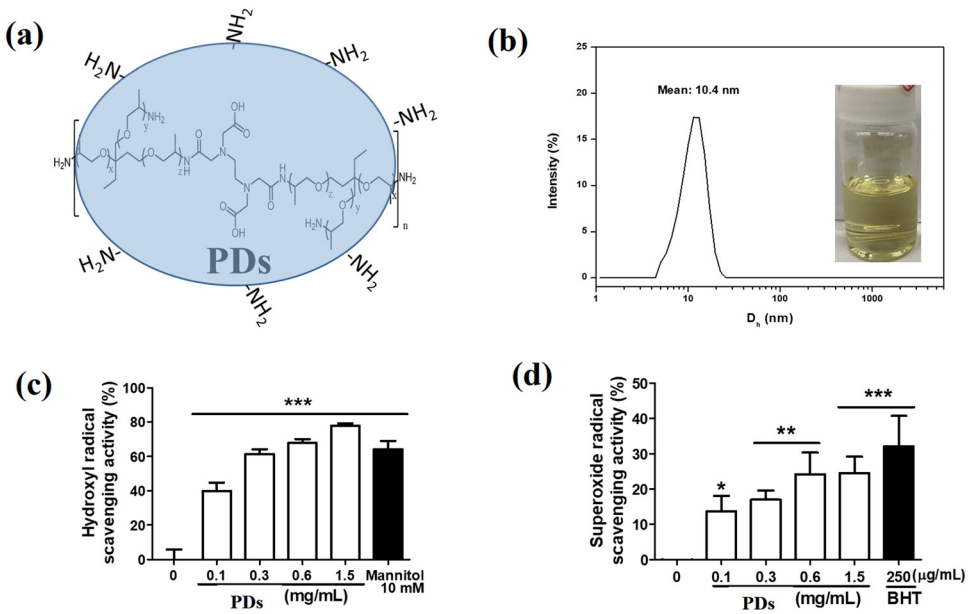

Fig. 1 (a) PD chemical structure. (b) DLS of the PD hydrogel in 5% PEG1000 aqueous solution photographs. (c) Hydroxyl radical scavenging activity of PDs. Mannitol at a concentration of 10 mM represents the positive control. (d) Superoxide radical scavenging activity of PDs. BHT at a concentration of 250 μg mL^{-1} represents the positive control. Significant difference *versus* control group: *$p < 0.05$; **$p < 0.01$; ***$p < 0.001$.

This narrow size distribution confirms the uniformity of the PD nanoparticles in the hydrogel formulation, which is crucial for ensuring consistent therapeutic effects.

Next, we evaluated the antioxidant activity of PDs by their ability to scavenge hydroxyl radicals and superoxide anion radicals. As shown in Fig. 1c, mannitol (10 mM) was employed as a positive control, demonstrating a scavenging activity of 59.4 ± 5.0%. In comparison, PDs exhibited dose-dependent hydroxyl radical scavenging activity, with efficiencies of 32.6 ± 3.1%, 53.4 ± 2.7%, 67.9 ± 2.3%, and 77.9 ± 1.2% at concentrations of 0.1, 0.3, 0.6, and 1.5 mg mL^{-1}, respectively (Fig. 1d). The superoxide anion scavenging activity reached a plateau at 0.6 mg mL^{-1}, suggesting saturation of the relevant scavenging mechanisms at this concentration. These findings demonstrate that PDs at the tested concentrations possess significant antioxidant capabilities, effectively both hydroxyl radicals and superoxide anions. These properties highlight their potential to mitigate oxidative stress, reduce inflammation, and enhance wound repair when applied in skincare.

Picosecond laser-induced optical breakdown (LIOB) in the skin

Optical coherence tomography (OCT) was employed to visualize the effects of picosecond laser treatment on the skin. Immediately after laser irradiation (day 0), OCT imaging revealed the formation of cavitation bubbles at the dermal–epidermal junction (Fig. 2a, red arrows), indicating the successful generation of laser-induced optical breakdown (LIOB). These cavitation bubbles appeared as discrete, hyporeflective spaces surrounded by hyperreflective boundaries, with an average diameter of 42.7 ± 6.3 μm and a density of approximately 18.4 ± 3.2 bubbles/mm^2. The bubbles were primarily located at a depth of 150–300 μm from the skin surface, corresponding to the dermal–epidermal junction, which is the optimal target zone for stimulating wound healing responses.

On day 3 post-treatment, the cavitation bubbles persisted, though they had decreased in size to an average diameter of 31.5 ± 5.4 μm (Fig. 2b, red arrows). Importantly, the surrounding tissue architecture remained intact, with no evidence of excessive thermal damage or necrosis. Measurements of the wound edge showed a decrease in edema from 534 μm to 420 μm and a reduced wound gap from 138 μm to 96 μm, demonstrating tissue recovery and initiation of the healing cascade. These findings confirm that the picosecond laser parameters used in this study (755 nm wavelength, 0.71 J cm^{-2} fluence, 750 ps pulse duration, and 500 pulses) effectively induced LIOB in the skin while minimizing collateral tissue damage. The persistence of cavitation bubbles for at least 3 days suggests a sustained mechanical stimulus that may contribute to enhanced wound healing through prolonged activation of mechanotransduction pathways.

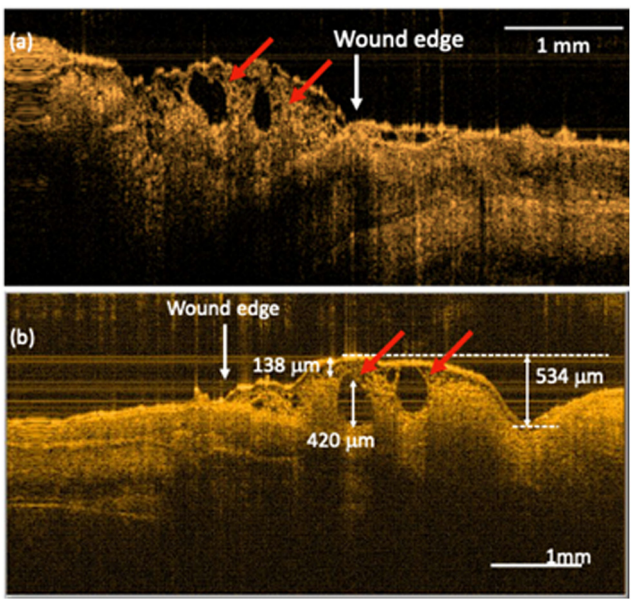

Fig. 2 Optical coherence tomography (OCT) analysis of cutaneous wound healing following picosecond laser treatment. OCT images of a cutaneous wound in nude mice: (a) immediately after wound creation (Day 0) and (b) at Day 3 post-treatment. Red arrows in (a) indicate the wound edge, showing initial disruption of the dermal structure. (b) Measurements showing a decrease in edema from 534 μm to 420 μm and a reduced wound gap from 138 μm, demonstrating tissue recovery and initiation of the healing cascade. Scale bar = 500 μm.

Macroscopic evaluation of wound healing

The progress of wound healing was monitored by capturing digital images of the wounds at various time points (days 0, 3, 6, 9, 12, 15, and 18) (Fig. 3). Qualitative assessment of these images revealed distinct healing patterns among the five experimental groups. On day 0, all wounds exhibited similar appearances immediately after creation, with well-defined circular defects of uniform size (6 mm diameter) surrounded by silicone splints to prevent contraction.

By day 3, wounds in the Control group exhibited the largest wound area, approximately 98.2 ± 4.1% of the initial wound size, with minimal signs of re-epithelialization and persistent inflammatory exudate. The PEG1000 group showed a moderate reduction in wound size (78.4 ± 5.3% of the initial size), likely due to the hydrating and protective effects of the vehicle on the wound bed (Fig. 4). The PD group demonstrated the most significant reduction in wound area (60.7 ± 6.2% of initial size), with noticeable re-epithelialization from the wound edges and reduced inflammatory exudate. This enhanced healing effect in the PD group can be attributed to the anti-inflammatory and antioxidant properties of PDs. The Laser and PDs + Laser groups exhibited slightly larger wound areas (90.1 ± 5.7% and 89.3 ± 4.9%, respectively) compared to the PD group, which could be a result of the initial controlled tissue disruption caused by the laser treatment.

By day 6, the differences between treatment groups became more pronounced. The Laser + PD group demonstrated the most significant reduction in wound size (49.6 ± 4.3% of the initial wound area), followed by the PD group (58.2 ± 5.1%) (Fig. 4). Both groups exhibited substantial re-epithelialization and the formation of healthy granulation tissue. The Laser and PEG1000 groups showed comparable wound sizes at this time point (68.5 ± 5.8% and 70.3 ± 6.2%, respectively), while the Control group continued to have the largest wounds (85.7 ± 5.4%). These observations

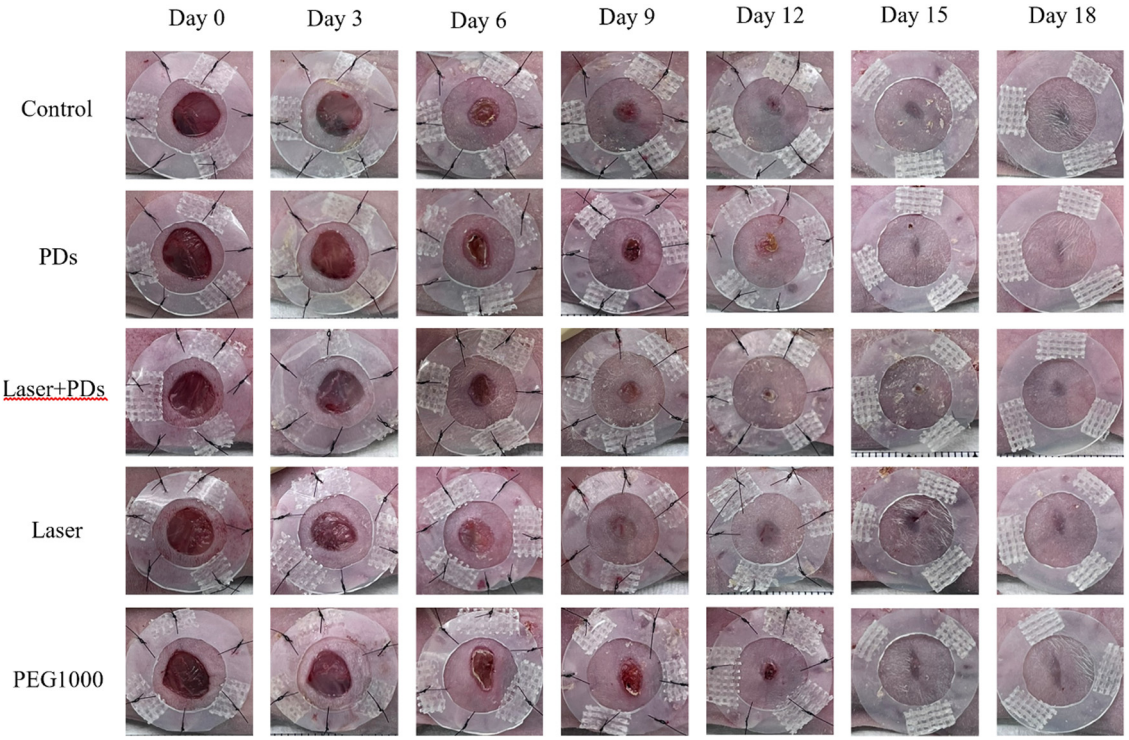

Fig. 3 Representative images of full-thickness wound healing progression in nude mice under various treatment conditions. Photographic timeline of full-thickness wound healing in nude mice over 18 days, comparing five treatment groups: Control, hyperbranched polymer dots (PDs), Laser + PDs, Laser alone, and polyethylene glycol 1000 (PEG1000). Images were captured on days 0, 3, 6, 9, 12, 15, and 18 post-wounding. Scale bar = 5 mm.

suggest that the combination of PDs and laser treatment provides synergistic benefits for wound healing, accelerating closure beyond what is achieved with either treatment alone.

On day 9, all treatment groups showed continued progress in wound healing, with the PDs + Laser group maintaining the smallest wound area (23.4 ± 3.7%), followed by the PD group (31.6 ± 4.2%), Laser group (42.3 ± 4.9%), PEG1000 group (46.7 ± 5.3%), and Control group (58.9 ± 6.1%). By day 12, wounds in the PDs + Laser group were nearly closed (6.2 ± 2.1%), while other groups showed varying degrees of wound closure: PDs (12.4 ± 3.3%), Laser (17.8 ± 3.9%), PEG1000 (24.5 ± 4.6%), and Control (35.2 ± 5.2%).

By day 15, wounds in the PDs + Laser and PD groups were completely closed, with the Laser group showing minimal residual wounds (2.1 ± 1.2%). The PEG1000 and Control groups still exhibited small unclosed areas (6.7 ± 2.5% and 12.3 ± 3.4%, respectively). On day 18, all wounds across all groups were completely closed, with varying scar appearances. The Laser + PD group exhibited the smallest and most well-defined scar, with minimal apparent contraction and a smoother surface. The PD and Laser groups showed slightly larger scars with moderate contraction, while the PEG1000 and Control groups had the largest and most visibly apparent scars with greater contraction and surface irregularity.

Quantitative analysis of wound closure

Quantitative assessment of wound closure through digital planimetry corroborated the macroscopic observations (Fig. 4). Statistical analysis using two-way ANOVA with Tukey's *post hoc* test revealed significant differences in wound closure rates among the treatment groups, particularly from day 3 to day 9. On day 3, the PD group demonstrated significantly improved wound closure compared to all other groups ($p < 0.001$ *vs.* Control and Laser, $p < 0.01$ *vs.* PEG1000 and PDs + Laser), suggesting an early anti-inflammatory effect of PDs.

The most striking differences were observed on day 6, where the PDs + Laser group exhibited significantly enhanced wound closure compared to all other groups ($p < 0.0001$). The percentage of the remaining wound area was 49.6 ± 4.3% for PDs + Laser, compared to 58.2 ± 5.1% for PDs, 68.5 ± 5.8% for Laser, 70.3 ± 6.2% for PEG1000, and 85.7 ± 5.4% for Control. This represents a 42.1% improvement in wound closure for the PDs + Laser group compared to the Control group. The synergistic effect of the combined therapy became evident at this time point, as the healing rate of the PD + Laser group exceeded the additive effects of the individual PD and Laser treatments.

Similarly, on day 9, the PDs + Laser group maintained superior wound closure (76.6 ± 3.7% closed) compared to all other groups ($p < 0.0001$ *vs.* Control, $p < 0.001$ *vs.* PEG1000 and Laser, $p < 0.05$ *vs.* PDs). The rate of wound closure, calculated as the percentage of the wound area closed per day between days 3 and 9, was significantly higher in the PDs + Laser group (11.0 ± 0.8% per day) compared to the PD group (8.6 ± 0.7% per day), Laser group (7.2 ± 0.6% per day), PEG1000 group (5.3 ± 0.5% per day), and Control group (4.6 ± 0.4% per day) ($p < 0.001$).

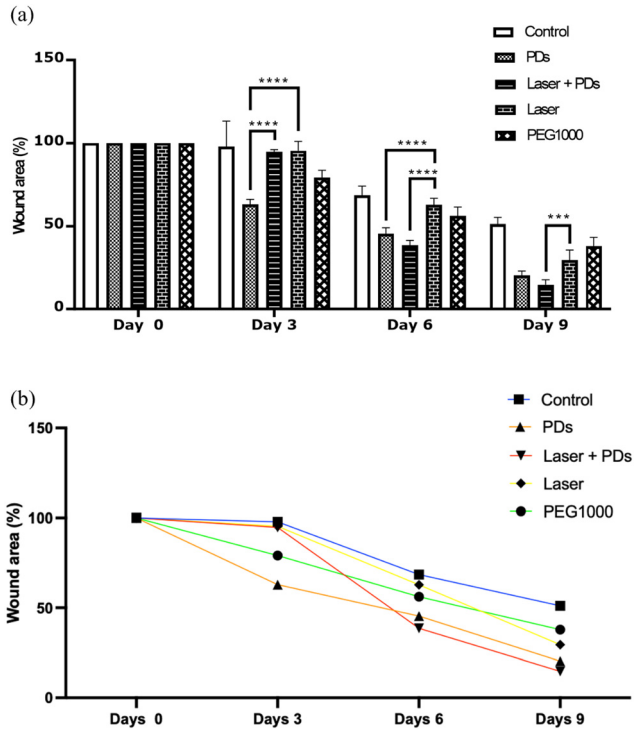

Fig. 4 Quantitative assessment of wound healing progression under different treatment conditions. (a) Bar graph representing the percentage of the wound area from day 0 to day 9 for each treatment group. (b) Line graph showing the rate of wound closure over time. Data are presented as mean ± SD. ****$p < 0.0001$ compared to Control (two-way ANOVA with Tukey's *post hoc* test). $n = 6$ per group.

These quantitative data demonstrate that the combination of PDs and picosecond laser treatment significantly accelerates wound closure compared to either treatment alone or no treatment. The enhanced wound healing effect of the combination therapy suggests synergistic mechanisms, potentially involving improved PD penetration through laser-created microchannels, complementary activation of distinct signaling pathways, and enhanced modulation of the wound healing environment.

Histological evaluation of wound healing

Immunohistochemical (IHC) staining was performed to evaluate the expression of key proteins involved in the wound healing process. On day 3, the Control and PEG1000 groups showed high expression levels of MAPK p38 and MMP-9 (Fig. 5A(a, e, f and j)), with the Control group displaying a large number of inflammatory cells (66.3 ± 7.2 cells per high-power field) and prominent scab formation at the wound edges (Fig. 5A(a and f)). Quantitative analysis of MAPK p38 expression revealed significantly higher levels in the Control (38.4 ± 4.2% positive area) and PEG1000 (35.7 ± 3.9% positive area) groups compared to the PD (17.3 ± 2.8%), Laser (22.6 ± 3.4%), and PDs + Laser (15.8 ± 2.5%) groups ($p < 0.001$). Similarly, MMP-9 expression was significantly elevated in the Control (42.7 ± 5.1%) and PEG1000 (39.5 ± 4.6%) groups compared to the PD (19.5 ± 3.1%), Laser (24.8 ± 3.7%), and PDs + Laser (16.9 ± 2.7%) groups ($p < 0.001$). In contrast, the PDs, Laser, and Laser + PD groups exhibited reduced MAPK p38 and MMP-9 expression (Fig. 5A(b–d and g–i)), indicating progression to the late inflammatory phase and entry into the tissue repair stage. The PDs + Laser group showed the lowest expression of both inflammatory markers ($p < 0.05$ *vs.* PD and Laser groups), suggesting a synergistic anti-inflammatory effect of the combination therapy. The reduced expression of these inflammatory markers corresponds with decreased inflammatory cell infiltration in these groups, with cell counts of 28.4 ± 4.5, 34.6 ± 5.2, and 22.7 ± 3.9 cells per high-power field in the PD, Laser, and PDs + Laser groups, respectively.

Fibronectin, an EMT marker and crucial component in wound healing, showed differential expression across treatment groups on day 3 (Fig. 5A(k–o)). Quantitative analysis revealed significantly higher fibronectin expression in the PD (32.6 ± 3.8%), Laser (27.4 ± 3.5%), and PDs + Laser (36.8 ± 4.1%) groups compared to the Control (12.3 ± 2.4%) and PEG1000 (15.7 ± 2.9%) groups ($p < 0.001$). The PDs + Laser group exhibited the highest fibronectin expression ($p < 0.05$ *vs.* Laser group), suggesting enhanced EMT activation in response to the combination therapy. This upregulation of fibronectin expression indicates active tissue regeneration and matrix remodeling in the treated groups, particularly in the PDs + Laser group. The elevated fibronectin levels correlate with the accelerated re-epithelialization observed in these groups, as fibronectin promotes keratinocyte migration during wound healing.

Angiogenesis assessment

The IHC results on day 6 (Fig. 5B) demonstrated varying degrees of neovascularization among the treatment groups. The Control and PEG1000 groups had only a small number of newly formed blood vessels in the superficial dermis, with average CD31-positive vessel counts of 4.2 ± 1.1 and 5.7 ± 1.3 per high-power field, respectively (Fig. 5B(a and e)). The PD group showed increased angiogenesis with 9.3 ± 1.6 CD31-positive vessels per high-power field (Fig. 5B(b)), while the Laser group exhibited 8.6 ± 1.5 vessels per high-power field (Fig. 5B(c)). The PDs + Laser group demonstrated the most pronounced CD31 expression, with 14.7 ± 2.2 CD31-positive vessels per high-power field (Fig. 5B(d)), significantly higher than all other groups ($p < 0.01$). Moreover, the CD31-positive vessels in the PDs + Laser group exhibited larger luminal diameters (15.4 ± 2.7 μm) compared to other groups (8.3 ± 1.8 μm in Control, 9.1 ± 2.0 μm in PEG1000, 11.7 ± 2.3 μm in PD, and 10.9 ± 2.1 μm in Laser), indicating more mature and functional vasculature.

CD34 expression, serving as a marker for stromal cells and fibroblasts involved in angiogenesis and tissue remodeling, showed similar patterns. CD34 expression was minimal in the Control group (7.6 ± 1.9% positive area, Fig. 5B(f)), while the PEG1000 group had increased CD34 expression (12.3 ± 2.4% positive area), primarily concentrated at the base of the dermis (Fig. 5B(j)). The PD (21.4 ± 3.2% positive area, Fig. 5B(g)), Laser (19.8 ± 3.0% positive area, Fig. 5B(h)), and PDs + Laser

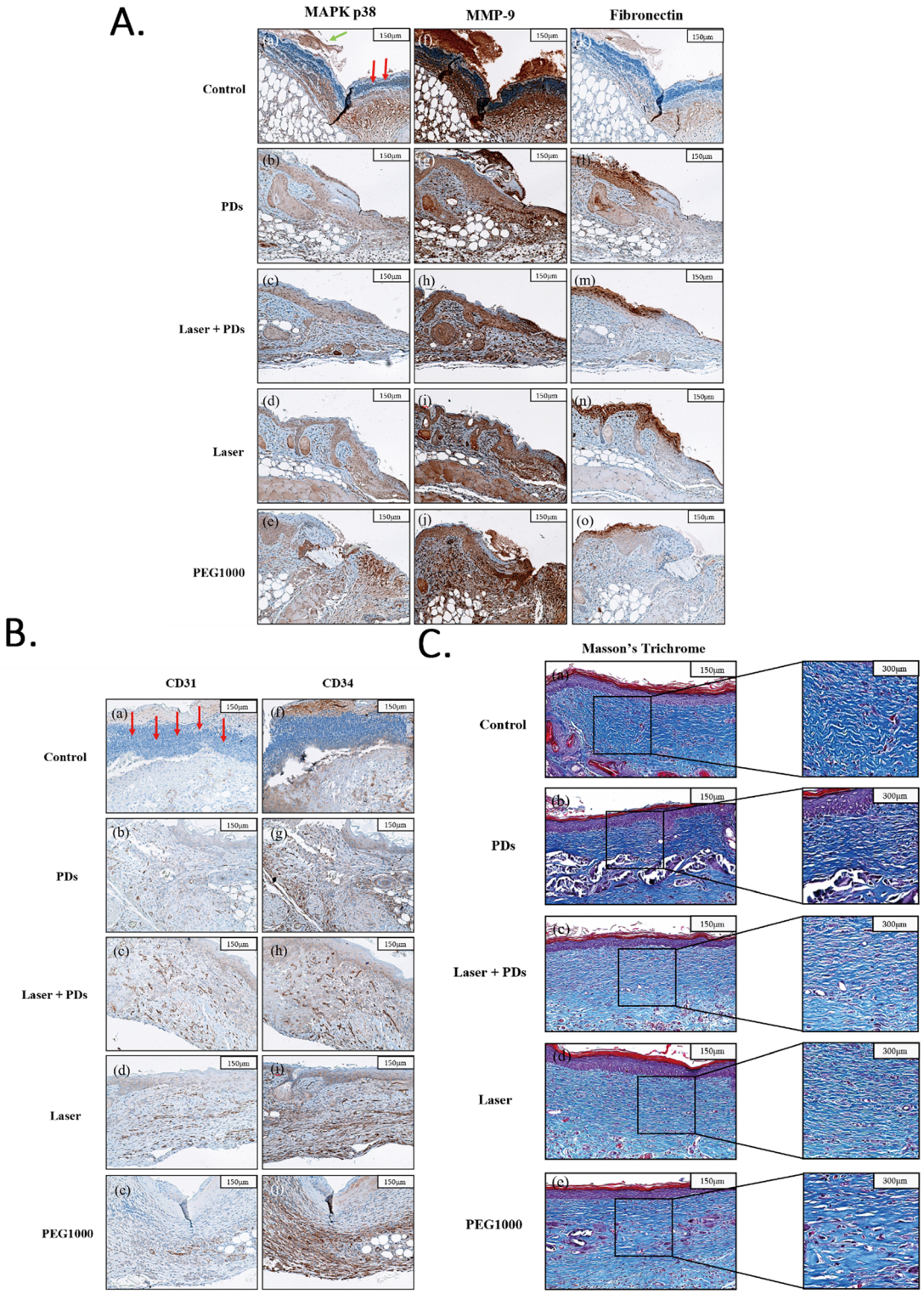

Fig. 5 Histological analysis of wound healing progression. (A) Immunohistochemical staining for MAPK p38 (a), (f) and (k), MMP-9 (b), (g) and (l), and fibronectin (c), (h) and (m) on day 3 post-wounding. Red arrows: inflammatory cells; green arrows: scab formation. Scale bar = 150 μm. (B) Immunohistochemical staining for CD31 (a)–(e) and CD34 (f)–(j) on day 6 post-wounding. Scale bar = 150 μm. (C) Masson's trichrome staining of wound tissues on day 18 post-wounding. Blue: collagen fibers; red/pink: cellular elements. Scale bar = 150 μm, insets = 300 μm.

(28.6 ± 3.7% positive area, Fig. 5B(i)) groups exhibited significantly higher CD34 expression ($p < 0.001$ *vs.* Control and PEG1000), with the PDs + Laser group showing the highest expression ($p < 0.05$ *vs.* PDs and Laser). The increased CD34 expression in the PDs + Laser group was distributed throughout the dermis, suggesting extensive neovascularization and tissue

restructuring around the wound. These findings indicate that the PDs + Laser combination therapy most effectively promotes angiogenesis and stem cell recruitment during the proliferative phase of wound healing, contributing to the accelerated wound closure observed in this group.

Collagen deposition and remodeling

Masson's trichrome (MT) staining on day 18 (Fig. 5C) revealed distinct patterns of collagen deposition and organization among the treatment groups. The Control and PEG1000 groups had large amounts of broad, randomly arranged, and loosely structured collagen fibers (Fig. 5C(a) and (e)), with collagen density measurements of 47.6 ± 5.3% and 52.4 ± 5.8%, respectively. The collagen fibers in these groups were predominantly thin (average fiber diameter: 2.3 ± 0.5 μm in Control and 2.7 ± 0.6 μm in PEG1000) and oriented in multiple directions, indicating immature scar formation.

In contrast, the PD, Laser, and Laser + PD groups exhibited more compact and orderly collagen fibers (Fig. 5C(b–d)), with collagen densities of 58.7 ± 6.1%, 61.3 ± 6.4%, and 67.9 ± 6.9%, respectively. The PDs + Laser group demonstrated the highest collagen density ($p < 0.05$ *vs.* all other groups) and the most organized collagen arrangement, with fibers predominantly aligned parallel to the skin surface. The collagen fibers in the PDs + Laser group were also thicker (average fiber diameter: 4.2 ± 0.7 μm) compared to the PD (3.6 ± 0.6 μm) and Laser (3.8 ± 0.7 μm) groups, indicating more mature collagen remodeling.

Semi-quantitative assessment of collagen organization using a scoring system (1–3) showed significantly higher scores in the PDs + Laser group (2.8 ± 0.3) compared to the PD (2.3 ± 0.3), Laser (2.4 ± 0.3), PEG1000 (1.6 ± 0.2), and Control (1.3 ± 0.2) groups ($p < 0.01$). These results indicate that the PDs + Laser combination therapy promotes more organized and mature collagen deposition, which is essential for optimal wound healing and reduced scarring.

Histomorphometric analysis of the dermal thickness revealed significant differences among groups. The PDs + Laser group exhibited a dermal thickness (1.24 ± 0.14 mm) closer to normal skin (1.32 ± 0.12 mm) compared to the PD (1.18 ± 0.12 mm), Laser (1.15 ± 0.13 mm), PEG1000 (1.02 ± 0.11 mm), and Control (0.94 ± 0.10 mm) groups. This indicates superior tissue regeneration in the PDs + Laser group, with dermal architecture more closely resembling normal skin.

Quantitative analysis of collagen expression and TGF-β signaling

ELISA results for type I collagen (Fig. 6a) showed that the Laser + PD group had the highest type I collagen expression (184.6 ± 16.8 ng mg^{-1} protein), followed by the Laser (153.7 ± 14.2 ng mg^{-1}), PD (142.3 ± 13.5 ng mg^{-1}), PEG1000 (165.2 ± 15.3 ng mg^{-1}), and Control (124.8 ± 12.9 ng mg^{-1}) groups. Statistical analysis revealed significant differences between the PDs + Laser group and the Control ($p < 0.001$), PD ($p < 0.01$), and Laser ($p < 0.05$) groups. Interestingly, the PEG1000 group exhibited unexpectedly high expression levels of type I collagen, which were significantly higher than those of the Control group ($p < 0.01$).

Type III collagen expression (Fig. 6b) followed a different pattern, with the PEG1000 group showing the highest levels (98.6 ± 10.2 ng mg^{-1}), followed by the Control (87.3 ± 9.7 ng mg^{-1}), Laser (74.5 ± 8.4 ng mg^{-1}), PD (69.8 ± 7.9 ng mg^{-1}), and PDs + Laser (65.2 ± 7.3 ng mg^{-1}) groups. The PEG1000 group had significantly higher type III collagen levels compared to the PD ($p < 0.01$), Laser ($p < 0.05$), and PDs + Laser ($p < 0.01$) groups. This elevated type III collagen expression in the PEG1000 group, combined with its high type I collagen levels, suggests excessive collagen production without proper maturation, potentially due to prolonged inflammation or dysregulated wound healing.

The type I/III collagen ratio (Fig. 6c), an important indicator of wound maturity and scar quality, was highest in the PDs + Laser group (2.83 ± 0.31), followed by the Laser (2.06 ± 0.24), PD (2.04 ± 0.23), Control (1.43 ± 0.19), and PEG1000 (1.68 ± 0.21) groups. The PDs + Laser group had a significantly higher type I/III collagen ratio compared to all other groups ($p < 0.01$ *vs.* PD and Laser, $p < 0.001$ *vs.* Control and PEG1000). This higher ratio indicates more mature collagen remodeling in the PDs + Laser group, with a predominance of type I collagen (associated with mature, strong scars) over type III collagen (associated with immature, weak scars).

Analysis of TGF-β signaling showed that the Laser and Laser + PD groups had the highest TGF-β levels (78.4 ± 8.2 pg mg^{-1}), significantly higher than the Laser (62.7 ± 7.1 pg mg^{-1}, $p < 0.05$), PD (58.3 ± 6.5 pg mg^{-1}, $p < 0.01$), PEG1000 (53.2 ± 6.0 pg mg^{-1}, $p < 0.01$), and Control (48.5 ± 5.8 pg mg^{-1}, $p < 0.001$) groups. Similarly, the PDs + Laser group exhibited the highest Smad2/3 expression (13.7 ± 1.6 ng mg^{-1}) compared to the Laser (10.8 ± 1.3 ng mg^{-1}, $p < 0.05$), PD (9.7 ± 1.2 ng mg^{-1}, $p < 0.01$), PEG1000 (8.5 ± 1.1 ng mg^{-1}, $p < 0.01$), and Control (7.6 ± 1.0 ng mg^{-1}, $p < 0.001$) groups (Fig. 6d). The enhanced TGF-β and Smad2/3 expression in the PDs + Laser group indicates stronger activation of the TGF-β/Smad signaling pathway, which is crucial for proper collagen synthesis and tissue remodeling during wound healing.

These results collectively demonstrate that the combination of PDs and picosecond laser treatment significantly enhances collagen remodeling and maturation through modulation of the TGF-β/Smad signaling pathway. The higher type I/III collagen ratio and enhanced TGF-β/Smad2/3 expression in the PDs + Laser group suggest that this combination therapy promotes more mature and organized collagen deposition, potentially resulting in better scar quality and mechanical properties.

Discussion

The present study demonstrates that the combination of hyperbranched polymer dots (PDs) and picosecond laser-induced optical breakdown (LIOB) significantly enhances wound healing outcomes through multiple synergistic mechanisms. Our findings reveal that this novel therapeutic approach accelerates

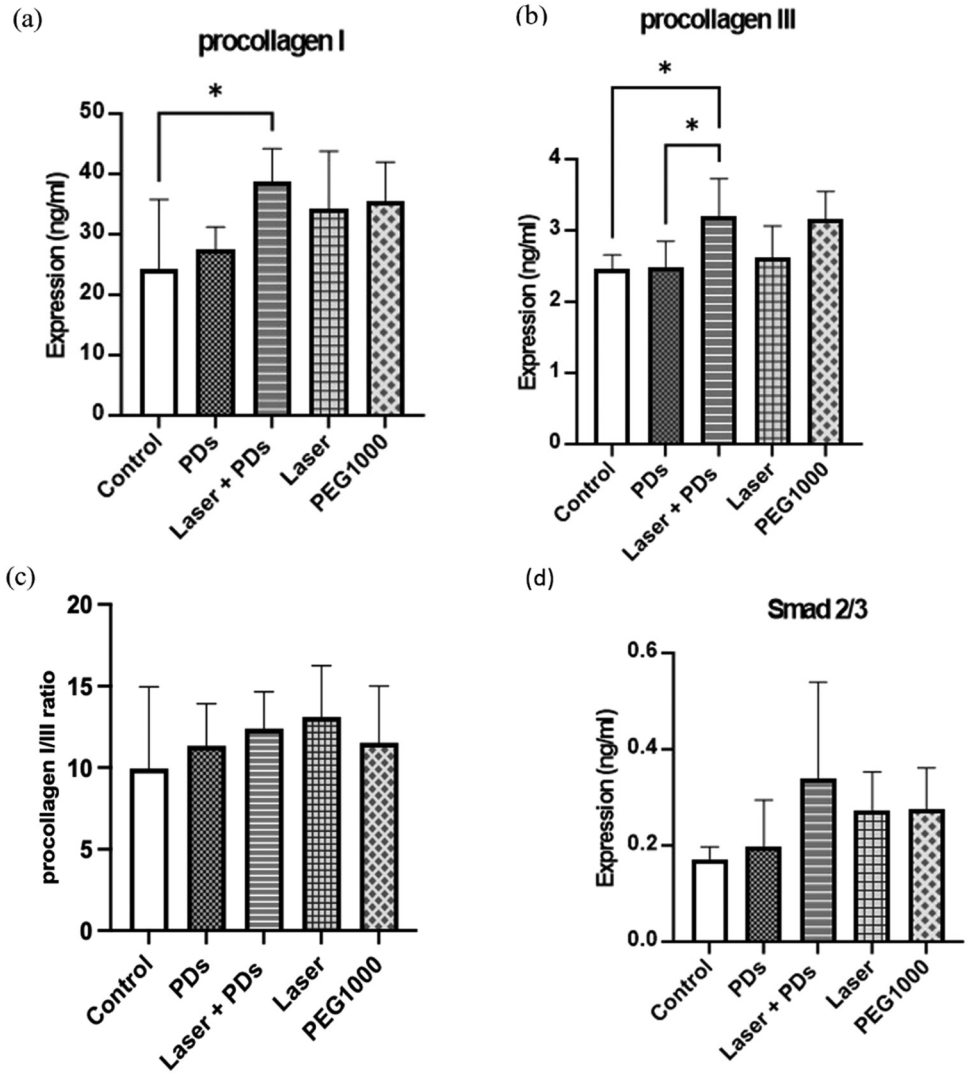

Fig. 6 Quantitative analysis of collagen expression and TGF-β signaling in wound tissues. ELISA results for (a) type I collagen, (b) type III collagen, (c) type I/III collagen ratio, and (d) Smad2/3 protein levels in wound tissue homogenates on day 18 post-wounding. Data are presented as mean ± SEM. *$p < 0.05$, **$p < 0.01$ compared to the control group (one-way ANOVA with Tukey's *post hoc* test). $n = 5$ for control group; $n = 6$ for all other groups.

wound closure, promotes organized collagen deposition, and modulates key molecular pathways involved in tissue regeneration.

The enhanced wound healing observed in the PDs + Laser group can be attributed to several complementary mechanisms. First, LIOB creates precisely controlled microchannels in the tissue, as evidenced by our OCT imaging results showing distinct cavitation bubbles at the dermal–epidermal junction with an average diameter of 42.7 ± 6.3 μm. This mechanical disruption likely serves two crucial functions: it facilitates LIOB-mediated dermal and epidermal regeneration and triggers mechanotransduction pathways that stimulate tissue repair. These findings aligns with recent work by Saha *et al.*, who demonstrated that controlled mechanical tissue disruption can activate mechanosensitive pathways, including YAP/TAZ signaling, that promote wound healing.[44] The persistence of these cavitation bubbles for at least three days, as observed in our OCT studies, suggests a sustained mechanical stimulus that may contribute to the prolonged activation of these regenerative pathways.

Our immunohistochemical analyses revealed that the PDs + Laser treatment significantly reduced MAPK p38 and MMP-9 expression compared to control groups, with positive staining areas of 15.8 ± 2.5% and 16.9 ± 2.7% respectively, indicating an accelerated transition from the inflammatory phase to the proliferative phase of wound healing. This modulation of inflammatory markers is particularly noteworthy, as chronic inflammation represents a major obstacle in treating non-healing wounds. The observed effect may be attributed to the anti-inflammatory properties of PDs, which have been previously reported to suppress pro-inflammatory cytokine production through regulation of NF-κB signaling.[45] Additionally, the antioxidant capabilities of PDs, as demonstrated by their hydroxyl radical scavenging activity (77.9 ± 1.2% at 1.5 mg mL^{-1}) and

superoxide anion scavenging activity (24.5 ± 4.7% at 1.5 mg mL^{-1}), likely contribute to the reduction of oxidative stress at the wound site, further attenuating inflammatory responses.

The significant increase in CD31 and CD34 expression in the PDs + Laser group (14.7 ± 2.2 vessels per high-power field and 28.6 ± 3.7% positive area, respectively) suggests enhanced angiogenesis, which is crucial for successful wound healing. The combination therapy appeared to create an optimal microenvironment for neovascularization, potentially through the synergistic effects of laser-induced tissue remodeling and the pro-angiogenic properties of PDs. These findings extend previous work by Chen *et al.*,[46] who showed that nanomaterial-based therapies could promote angiogenesis in chronic wounds, but our approach demonstrates superior outcomes through the integration of PDs + LIOB technology. The increased vessel diameter (15.4 ± 2.7 μm) observed in the PDs + Laser group compared to other groups indicates more mature and functional vasculature, essential for efficient nutrient and oxygen delivery to the healing tissue.

A particularly significant finding was the improved collagen organization and more favorable type I/III collagen ratio observed in the PDs + Laser group. The Masson's trichrome staining revealed more compact and orderly collagen fibers with greater density (67.9 ± 6.9%) and thickness (4.2 ± 0.7 μm), suggesting better quality tissue regeneration with potentially reduced scarring. This outcome may be attributed to the enhanced Smad2/3 expression (13.7 ± 1.6 ng mg^{-1}) observed in our ELISA results, indicating optimal activation of the TGF-β signaling pathway. These results align with recent work by Deng *et al.*,[5] who demonstrated that controlled modulation of TGF-β signaling is crucial for minimizing scar formation while promoting tissue regeneration.

The superior wound closure rates observed in the combination therapy group (50.4% reduction by day 6 compared to only 14.3% in controls, $p < 0.0001$) suggest that the LIOB-mediated dermal and epidermal regeneration creates an optimal therapeutic window for wound healing. The picosecond laser's ultrafast pulses appear to enhance the bioavailability of PDs while minimizing collateral thermal damage, as evidenced by our OCT findings. This represents a significant advancement over conventional wound treatments, which often struggle with achieving adequate therapeutic concentrations in the wound bed while avoiding tissue damage.

Our mechanistic studies reveal that the combination therapy enhances wound healing through multiple pathways: (1) PDs' bioactivity, including antioxidant properties that effectively reduce oxidative stress; (2) LIOB-mediated dermal and epidermal regeneration through controlled microchannel formation; (3) modulation of inflammatory responses through reduced MAPK p38 and MMP-9 expression, (4) enhanced angiogenesis as evidenced by increased CD31 and CD34 expression, and (5) optimal collagen remodeling through regulated TGF-β/Smad signaling.

The molecular mechanisms underlying this synergistic effect likely involve the complementary activation of distinct signaling pathways. While LIOB primarily activates the TGF-β/Smad-dependent pathway, as evidenced by increased TGF-β (78.4 ± 8.2 pg mg^{-1}) and Smad2/3 levels, PDs appear to function through the non-Smad p38 MAPK/Snail axis to enhance EMT, as indicated by the upregulation of fibronectin (36.8 ± 4.1% positive area). This dual-pathway activation provides a comprehensive approach to wound healing, addressing both matrix remodeling and re-epithelialization aspects of the process. Furthermore, the LIOB-created microchannels likely enhance PD penetration into the wound bed, improving their bioavailability and therapeutic efficacy. This physical enhancement of drug delivery represents a novel mechanism of synergy between these two treatment modalities.

The findings from this study have important clinical implications. The combination of PDs and LIOB represents a promising strategy for treating chronic wounds, which often prove resistant to conventional therapies. The nude mouse model used in this study offers translational relevance due to its epidermal structure and wound healing kinetics that closely resemble human cutaneous wound repair.[36,41] While we acknowledge that the nude mouse model has limitations, particularly regarding differences in immune response compared to immunocompetent models, it provides valuable insights into the fundamental mechanisms of wound healing and allows for clear assessment of therapeutic interventions with minimal interference from adaptive immune responses.[32,36]

Several limitations of this study should be acknowledged. While our nude mouse model provided valuable insights into the healing mechanisms, future studies should validate these findings in diabetic wound models and other clinically relevant conditions that represent the complex pathophysiology of chronic wounds in humans. Additionally, long-term follow-up studies are needed to fully assess the durability of the improved healing outcomes and evaluate any potential adverse effects. The role of PDs in modulating bacterial biofilms, which are frequently present in chronic wounds, was not addressed in the current study and merits investigation in future research.

The optimization of treatment parameters represents another area for future research. The laser parameters (755 nm wavelength, 0.71 J cm^{-2} fluence, 750 ps pulse duration, and 500 pulses) and PD concentration (5 mg mL^{-1}) used in this study were selected based on preliminary experiments and previous literature. However, systematic optimization of these parameters for specific wound types and patient-specific conditions could further enhance therapeutic efficacy. Studies exploring the effects of varying pulse numbers, fluence levels, and PD concentrations would provide valuable insights for clinical translation.

The unexpectedly high collagen expression observed in the PEG1000 group warrants further investigation. This finding suggests that PEG1000 may have intrinsic effects on collagen synthesis, potentially through hydration-mediated mechanisms or by directly influencing fibroblast activity. Understanding these effects is important for optimizing vehicle formulations in wound healing applications.

Future research directions should focus on developing specialized PD formulations for specific wound types, optimizing

the laser parameters for different clinical scenarios, investigating the potential for sequential or repeated treatments, and exploring the combination of this approach with other therapeutic agents, such as growth factors or stem cells. Studies in larger animal models with a skin architecture more similar to humans, such as porcine models, would provide additional translational insights. Furthermore, investigating the effects of PDs + LIOB therapy on other aspects of wound healing, such as bacterial biofilm disruption, immune cell recruitment, and the activation of endogenous stem cells, would enhance our understanding of this promising therapeutic approach.

Conclusions

The present study provides compelling evidence that the synergistic integration of laser-induced optical breakdown (LIOB) and hyperbranched polymer dots (PDs) represents a transformative strategy for enhancing wound healing through both biomechanical and biochemical modulation. By leveraging the distinct yet complementary mechanisms of these two approaches, this study demonstrates how LIOB-mediated mechanotransduction and PD-driven antioxidant and anti-inflammatory effects converge to accelerate wound closure, promote extracellular matrix (ECM) remodeling, and restore skin integrity with minimal fibrosis.

The mechanistic insights gained from this investigation establish a strong foundation for understanding how LIOB and PDs interact at both the molecular and cellular levels. LIOB was found to significantly enhance the activation of the TGF-β/Smad pathway, promoting fibroblast proliferation and ECM synthesis, while simultaneously facilitating PD penetration into deeper tissue layers through the formation of transient microchannels within the wound bed. PDs, on the other hand, exerted potent reactive oxygen species (ROS) scavenging activity, mitigating oxidative stress and reducing the inflammatory burden that often impairs efficient wound repair. Additionally, PDs activated TGF-β non-Smad signaling *via* p38 MAPK/Snail, promoting epithelial–mesenchymal transition (EMT), which is crucial for keratinocyte migration and re-epithelialization. The interplay between these pathways underscores a novel paradigm wherein LIOB augments the biological efficacy of PDs by improving their bioavailability while simultaneously triggering mechanosensitive signaling cascades that further contribute to tissue regeneration.

Histological and molecular analyses corroborated these findings, demonstrating that wounds treated with LIOB-PD combination therapy exhibited faster re-epithelialization, reduced inflammation, increased fibroblast activation, and enhanced collagen organization, compared to either treatment alone. The increased expression of fibronectin, vimentin, and α-smooth muscle actin (α-SMA) in the combination therapy group further supports the hypothesis that PDs promote granulation tissue formation, while LIOB facilitates fibroblast migration and matrix deposition. Importantly, the reduction in pro-inflammatory cytokines such as TNF-α and IL-6 highlights the anti-inflammatory properties of PDs, which contribute to a more favorable wound microenvironment.

From a translational perspective, these findings have significant implications for advancing minimally invasive, nanotechnology-enhanced wound healing therapies. The ability of LIOB to enhance PD penetration without compromising epidermal integrity suggests a potential clinical advantage in non-pharmacological interventions for acute and chronic wounds. Furthermore, the observed improvements in ECM organization and barrier function restoration, as evidenced by decreased transepidermal water loss (TEWL), indicate that this combination therapy not only accelerates wound closure but also enhances tissue quality and functional recovery.

Despite the promising outcomes of this study, certain limitations must be acknowledged. While the nude mouse model provides a well-characterized platform for investigating cutaneous wound healing, it does not fully recapitulate the immunological complexities of chronic wounds, particularly those associated with diabetes or compromised immune functions. Future investigations will focus on evaluating the LIOB-PD synergy in diabetic and immunocompetent wound models to bridge the translational gap and enhance clinical relevance. Additionally, further optimization of laser parameters and PD formulations will be essential to fine-tune their therapeutic potential while minimizing potential off-target effects.

In conclusion, this study establishes LIOB-assisted PD therapy as a novel and highly effective approach for promoting wound healing. By integrating biomechanical modulation with nanotechnology-driven biochemical interventions, this strategy offers a promising alternative to conventional wound care approaches. The mechanistic insights gained from this work provide a solid foundation for future clinical translation, with potential applications in post-surgical recovery, chronic wound management, and regenerative medicine. With continued research and optimization, LIOB-PD therapy has the potential to revolutionize the field of advanced wound healing technologies, offering a highly targeted, non-invasive, and efficacious treatment paradigm that addresses multiple facets of wound pathophysiology simultaneously.

Author contributions

All authors had full access to all the data in the study and take responsibility for the integrity of the data and the accuracy of the data analysis. Data curation and methodology: C.-C. Chang, H.-M. Iao, S.-C. Fan, Y.-H. Tu, J.-C. Siew, K.-C. Ma, Y.-H. Lee, H.-M. Chiang, and C.-C. Cheng; conceptualization, writing – original draft preparation, writing – review and editing, and project administration: T.-Y. Juang.

Data availability

The data supporting the findings of this study are available from the corresponding author upon reasonable request.

Conflicts of interest

The authors declare no conflicts of interest relevant to this study.

Acknowledgements

NSTC 112-2221-E-039-006-MY2, MOST 111-2314-*B*-039-069, CMU111-S-08, CMU111-ASIA-11, CMU112-MF-66, and CMU113-MF-68.

References

1 C. K. Sen, Human Wound and Its Burden: Updated 2022 Compendium of Estimates, *Adv. Wound Care*, 2023, **12**(12), 657–670, DOI: **10.1089/wound.2023.0150**.

2 R. G. Frykberg and J. Banks, Challenges in the Treatment of Chronic Wounds, *Adv. Wound Care*, 2015, **4**(9), 560–582, DOI: **10.1089/wound.2015.0635**.

3 N. G. Frangogiannis, The role of transforming growth factor (TGF)-β in the infarcted myocardium, *J. Thorac. Dis.*, 2017, **9**(1), S52–s63 From NLM. Y. Inagaki and I. Okazaki, Emerging insights into Transforming growth factor β Smad signal in hepatic fibrogenesis, *Gut*, 2007, **56**(2), 284–292, DOI: **10.1136/gut.2005.088690%JGut**.

4 A. O. Giarratana, C. M. Prendergast, M. M. Salvatore and K. M. Capaccione, TGF-β signaling: critical nexus of fibrogenesis and cancer, *J. Transl. Med.*, 2024, **22**(1), 594, DOI: **10.1186/s12967-024-05411-4**.

5 Z. Deng, T. Fan, C. Xiao, H. Tian, Y. Zheng, C. Li and J. He, TGF-β signaling in health, disease and therapeutics, *Signal Transduction Targeted Ther.*, 2024, **9**(1), 61, DOI: **10.1038/s41392-024-01764-w**.

6 S. Preetam, A. Ghosh, R. Mishra, A. Pandey, D. S. Roy, S. Rustagi and S. Malik, Electrical stimulation: a novel therapeutic strategy to heal biological wounds, *RSC Adv.*, 2024, **14**(44), 32142–32173, DOI: **10.1039/D4RA04258A**; Y. Ju, Y. Luo, R. Li, W. Zhang, Y. Ge and J. Tang, Multifunctional combined drug-loaded nanofibrous dressings with anti-inflammatory, antioxidant stress and microenvironment improvement for diabetic wounds, *RSC Adv.*, 2024, **14**(40), 29606–29623, DOI: **10.1039/D4RA04860A**; M. Khalid, F. Jameel, T. Jabri, A. Jabbar, A. Salim, I. Khan and M. R. Shah, α-Terpineol loaded, electron beam crosslinked polyvinyl alcohol/tapioca starch hydrogel sheets; fabrication, characterization and evaluation of wound healing potential on a full thickness acid burn wound, *RSC Adv.*, 2024, **14**(38), 28058–28076, DOI: **10.1039/D4RA04572F**.

7 J. H. Kim, B. Yang, A. Tedesco, E. G. D. Lebig, P. M. Ruegger, K. Xu, J. Borneman and M. Martins-Green, High Levels of Oxidative Stress and Skin Microbiome are Critical for Initiation and Development of Chronic Wounds in Diabetic Mice, *Sci. Rep.*, 2019, **9**(1), 19318, DOI: **10.1038/s41598-019-55644-3** From NLM Medline.

8 S. Dhall, D. C. Do, M. Garcia, J. Kim, S. H. Mirebrahim, J. Lyubovitsky, S. Lonardi, E. A. Nothnagel, N. Schiller and M. Martins-Green, Generating and reversing chronic wounds in diabetic mice by manipulating wound redox parameters, *J. Diabetes Res.*, 2014, 562625, DOI: **10.1155/2014/562625** From NLM Medline.

9 S. Dhall, D. Do, M. Garcia, D. S. Wijesinghe, A. Brandon, J. Kim, A. Sanchez, J. Lyubovitsky, S. Gallagher and E. A. Nothnagel, *et al.*, A novel model of chronic wounds: importance of redox imbalance and biofilm-forming bacteria for establishment of chronicity, *PLoS One*, 2014, **9**(10), e109848, DOI: **10.1371/journal.pone.0109848** From NLM Medline.

10 Y. Dong and Z. Wang, ROS-scavenging materials for skin wound healing: advancements and applications, *Front. Bioeng. Biotechnol.*, 2023, **11**, 1304835, DOI: **10.3389/fbioe.2023.1304835**, From NLM PubMed-not-MEDLINE F. Xu, C. Zhang and D. T. Graves, Abnormal cell responses and role of TNF-alpha in impaired diabetic wound healing, *Biomed. Res. Int.*, 2013, 754802, DOI: **10.1155/2013/754802**, From NLM Medline.

11 F. B. Lopes, M. M. Sarandy, R. D. Novaes, G. Valacchi and R. V. Goncalves, OxInflammatory Responses in the Wound Healing Process: A Systematic Review, *Antioxidants*, 2024, **13**(7), 823, DOI: **10.3390/antiox13070823**. From NLM PubMed-not-MEDLINE F. Cialdai, C. Risaliti and M. Monici, Role of fibroblasts in wound healing and tissue remodeling on Earth and in space, *Front Bioeng. Biotechnol.*, 2022, **10**, 958381, DOI: **10.3389/fbioe.2022.958381** From NLM PubMed-not-MEDLINE C. Dunnill, T. Patton, J. Brennan, J. Barrett, M. Dryden, J. Cooke, D. Leaper and N. T. Georgopoulos, Reactive oxygen species (ROS) and wound healing: the functional role of ROS and emerging ROS-modulating technologies for augmentation of the healing process, *Int. Wound J.*, 2017, **14**(1), 89–96, DOI: **10.1111/iwj.12557** From NLM Medline M. Hunt, M. Torres, E. Bachar-Wikstrom and J. D. Wikstrom, Cellular and molecular roles of reactive oxygen species in wound healing, *Commun. Biol.*, 2024, **7**(1), 1534, DOI: **10.1038/s42003-024-07219-w** From NLM Medline.

12 X. Qu, C. Gao, L. Fu, Y. Chu, J.-H. Wang, H. Qiu and J. Chen, Positively Charged Carbon Dots with Antibacterial and Antioxidant Dual Activities for Promoting Infected Wound Healing, *ACS Appl. Mater. Interfaces*, 2023, **15**(15), 18608–18619, DOI: **10.1021/acsami.2c21839**; N. N. Shershakova, S. M. Andreev, A. A. Tomchuk, E. A. Makarova, A. A. Nikonova, E. A. Turetskiy, O. A. Petukhova, O. Y. Kamyshnikov, O. I. Ivankov and O. A. Kyzyma, *et al.*, Wound healing activity of aqueous dispersion of fullerene C60 produced by "green technology", *Nanomed.: Nanotechnol., Biol. Med.*, 2023, **47**, 102619, DOI: **10.1016/j.nano.2022.102619**.

13 J. Liu, R. Li and B. Yang, Carbon dots: a new type of carbon-based nanomaterial with wide applications, *ACS Cent. Sci.*, 2020, **6**(12), 2179–2195; S. Tao, S. Zhu, T. Feng, C. Zheng and B. Yang, Crosslink-enhanced emission effect on luminescence in polymers: advances and perspectives, *Angew. Chem.*, 2020, **132**(25), 9910–9924.

14 Z. Wang, L. Liu, W. Bu, M. Zheng, N. Jin, K. Zhang, X. Xu, D. Zhou, B. Yang and H. Sun, Carbon Dots Induce Epithelial-Mesenchymal Transition for Promoting

Cutaneous Wound Healing via Activation of TGF-β/p38/Snail Pathway, *Adv. Funct. Mater.*, 2020, **30**(43), 2004886, DOI: **10.1002/adfm.202004886**.

15 N. Tang, Z. Ding, J. Zhang, Y. Cai and X. Bao, Recent advances of antioxidant low-dimensional carbon materials for biomedical applications, *Front Bioeng. Biotechnol.*, 2023, **11**, 1121477, DOI: **10.3389/fbioe.2023.1121477** From NLM PubMed-not-MEDLINE H. Sun, A. Zhao, N. Gao, K. Li, J. Ren and X. Qu, Deciphering a nanocarbon-based artificial peroxidase: chemical identification of the catalytically active and substrate-binding sites on graphene quantum dots, *Angew. Chem., Int. Ed.*, 2015, **54**(24), 7176–7180, DOI: **10.1002/anie.201500626** NLMMedline From.

16 Z. Ji, A. Sheardy, Z. Zeng, W. Zhang, H. Chevva, K. Allado, Z. Yin and J. Wei, Tuning the Functional Groups on Carbon Nanodots and Antioxidant Studies, *Molecules*, 2019, **24**(1), 152, DOI: **10.3390/molecules24010152** From NLM Medline M. Mabrouk, D. B. Das, Z. A. Salem and H. H. Beherei, Nanomaterials for Biomedical Applications: Production, Characterisations, Recent Trends and Difficulties, *Molecules*, 2021, **26**(4), 1077, DOI: **10.3390/molecules26041077** From NLM Medline S. Zhu, Q. Meng, L. Wang, J. Zhang, Y. Song, H. Jin, K. Zhang, H. Sun, H. Wang and B. Yang, Highly photoluminescent carbon dots for multicolor patterning, sensors, and bioimaging, *Angew. Chem., Int. Ed.*, 2013, **52**(14), 3953–3957, DOI: **10.1002/anie.201300519** From NLM Medline.

17 W. Liao, J. Lin, W. Wang, M. Zhang, Y. Chen, X. Li, H. Liu, P. X. Wang, G. Zhao and J. Fu, *et al.*, Assembly of ceria-Nrf2 nanoparticles as macrophage-targeting ROS scavengers protects against myocardial infarction, *Front Pharmacol.*, 2025, **15**, 1503757, DOI: **10.3389/fphar.2024.1503757** From NLM PubMed-not-MEDLINE S. Saha, N. Sachivkina, A. Karamyan, E. Novikova and T. Chubenko, Advances in Nrf2 Signaling Pathway by Targeted Nanostructured-Based Drug Delivery Systems, *Biomedicines*, 2024, **12**(2), 403, DOI: **10.3390/biomedicines12020403** From NLM PubMed-not-MEDLINE L. Lin, Q. Wu, F. Lu, J. Lei, Y. Zhou, Y. Liu, N. Zhu, Y. Yu, Z. Ning and T. She, *et al.*, Nrf2 signaling pathway: current status and potential therapeutic targetable role in human cancers, *Front Oncol.*, 2023, **13**, 1184079, DOI: **10.3389/fonc.2023.1184079** From NLM PubMed-not-MEDLINE.

18 C.-K. Liu, F.-Y. Su, T.-Y. Juang and Y.-C. Liu, Sustained antibacterial release of zwitterionic globular hyperbranched polymer dots intercalated into layered double hydroxides, *RSC Adv.*, 2024, **14**(43), 31694–31703, DOI: **10.1039/D4RA05587J**.

19 Y.-Y. Chen, S.-C. Fan, C.-C. Chang, J.-C. Wang, H.-M. Chiang and T.-Y. Juang, Non-Conventional Fluorescence and Cytotoxicity of Two Aliphatic Hyperbranched Polymer Dots Having Poly(amic acid) Structures: Implications for Labeling Nanodrug Carriers, *ACS Omega*, 2021, **6**(48), 33159–33170, DOI: **10.1021/acsomega.1c05537**.

20 C.-C. Chang, Y.-Y. Chen, H.-M. Chiang, Y.-F. Shen, J.-C. Wang, K.-C. Ma, C.-H. Lin and T.-Y. Juang, Nonconventional Fluorescent Hyperbranched Polymer Dots as Skin Nanocarriers Constructed from an Olefinic Aliphatic AB2-Type Monomer, *ACS Appl. Polym. Mater.*, 2022, **4**(10), 7790–7800, DOI: **10.1021/acsapm.2c01328**.

21 Y. E. Zhang, Non-Smad pathways in TGF-beta signaling, *Cell. Res.*, 2009, **19**(1), 128–139, DOI: **10.1038/cr.2008.328** From NLM Medline A. Ahmadi, M. Najafi, B. Farhood and K. Mortezaee, Transforming growth factor-beta signaling: Tumorigenesis and targeting for cancer therapy, *J. Cell. Physiol.*, 2019, **234**(8), 12173–12187, DOI: **10.1002/jcp.27955** From NLM Medline.

22 F. Cheng, Y. Shen, P. Mohanasundaram, M. Lindstrom, J. Ivaska, T. Ny and J. E. Eriksson, Vimentin coordinates fibroblast proliferation and keratinocyte differentiation in wound healing via TGF-beta-Slug signaling, *Proc. Natl., Acad. Sci. U. S. A.*, 2016, **113**(30), E4320–4327, DOI: **10.1073/pnas.1519197113** From NLM Medline C. Yan, W. A. Grimm, W. L. Garner, L. Qin, T. Travis, N. Tan and Y. P. Han, Epithelial to mesenchymal transition in human skin wound healing is induced by tumor necrosis factor-alpha through bone morphogenic protein-2, *Am. J. Pathol.*, 2010, **176**(5), 2247–2258, DOI: **10.2353/ajpath.2010.090048** From NLM Medline M. Zeisberg and E. G. Neilson, Biomarkers for epithelial-mesenchymal transitions, *J. Clin. Invest.*, 2009, **119**(6), 1429–1437, DOI: **10.1172/JCI36183** From NLM Medline.

23 C. Liu, P.-J. Wu, S.-H. Chia, C.-K. Sun and Y.-H. Liao, Characterization of picosecond laser-induced optical breakdown using harmonic generation microscopy, *Lasers Surg. Med.*, 2023, **55**(6), 561–567, DOI: **10.1002/lsm.23664**; K. C. Flanders, C. D. Major, A. Arabshahi, E. E. Aburime, M. H. Okada, M. Fujii, T. D. Blalock, G. S. Schultz, A. Sowers and M. A. Anzano, *et al.*, Interference with Transforming Growth Factor-β/Smad3 Signaling Results in Accelerated Healing of Wounds in Previously Irradiated Skin, *Am. J. Pathol.*, 2003, **163**(6), 2247–2257, DOI: **10.1016/S0002-9440(10)63582-1**; Y.-J. Wang, E.-T. Lin, Y.-T. Chen, P.-C. Chiu, B.-S. Lin, H.-M. Chiang, Y.-H. Huang, K.-Y. Wang, H.-Y. Lin and T.-M. Chang, *et al.*, Prospective randomized controlled trial comparing treatment efficacy and tolerance of picosecond alexandrite laser with a diffractive lens array and triple combination cream in female asian patients with melasma, *J. Eur. Acad. Dermatol. Venereol.*, 2020, **34**(3), 624–632, DOI: **10.1111/jdv.15934**.

24 Y. Zhou, M. R. Hamblin and X. Wen, An update on fractional picosecond laser treatment: histology and clinical applications, *Lasers Med. Sci.*, 2023, **38**(1), 45, DOI: **10.1007/s10103-022-03704-y** From NLM Medline.

25 L. Habbema, R. Verhagen, R. Van Hal, Y. Liu and B. Varghese, Minimally invasive non-thermal laser technology using laser-induced optical breakdown for skin rejuvenation, *J. Biophotonics*, 2012, **5**(2), 194–199, DOI: **10.1002/jbio.201100083** From NLM Medline J. A. Brauer, V. Kazlouskaya, H. Alabdulrazzaq, Y. S. Bae, L. J. Bernstein, R. Anolik, P. A. Heller and R. G. Geronemus, Use of a picosecond pulse duration laser with specialized optic for treatment of facial acne scarring, *JAMA Dermatol.*, 2015,

151(3), 278–284, DOI: 10.1001/jamadermatol.2014.3045 From NLM Medline E. A. Tanghetti, The histology of skin treated with a picosecond alexandrite laser and a fractional lens array, *Lasers Surg. Med.*, 2016, **48**(7), 646–652, DOI: 10.1002/lsm.22540 From NLM Medline.

26 V. Mehta, K. L. Pang, C. S. Givens, Z. Chen, J. Huang, D. T. Sweet, H. Jo, J. S. Reader and E. Tzima, Mechanical forces regulate endothelial-to-mesenchymal transition and atherosclerosis via an Alk5-Shc mechanotransduction pathway, *Sci. Adv.*, 2021, **7**(28), eabg5060, DOI: 10.1126/sciadv.abg5060 From NLM PubMed-not-MEDLINE.

27 X. Cai, K. C. Wang and Z. Meng, Mechanoregulation of YAP and TAZ in Cellular Homeostasis and Disease Progression, *Front Cell. Dev. Biol.*, 2021, **9**, 673599, DOI: 10.3389/fcell.2021.673599 From NLM PubMed-not-MEDLINE.

28 S. Dupont, L. Morsut, M. Aragona, E. Enzo, S. Giulitti, M. Cordenonsi, F. Zanconato, J. Le Digabel, M. Forcato and S. Bicciato, *et al.*, Role of YAP/TAZ in mechanotransduction, *Nature*, 2011, **474**(7350), 179–183, DOI: 10.1038/nature10137 From NLM Medline S. Piccolo, S. Dupont and M. Cordenonsi, The biology of YAP/TAZ: hippo signaling and beyond, *Physiol. Rev.*, 2014, **94**(4), 1287–1312, DOI: 10.1152/physrev.00005.2014 From NLM Medline Y. Deng, J. Lu, W. Li, A. Wu, X. Zhang, W. Tong, K. K. Ho, L. Qin, H. Song and K. K. Mak, Reciprocal inhibition of YAP/TAZ and NF-kappaB regulates osteoarthritic cartilage degradation, *Nat. Commun.*, 2018, **9**(1), 4564, DOI: 10.1038/s41467-018-07022-2 From NLM Medline.

29 J. Baleisis and R. Rudys, Microlesion healing dynamics in in vivo porcine skin after treatment with 1064 nm picosecond-domain Nd:YAG laser, *J. Biophotonics*, 2023, **16**(4), e202200349, DOI: 10.1002/jbio.202200349 From NLM Medline.

30 G. Apodaca, Modulation of membrane traffic by mechanical stimuli, *Am. J. Physiol.: Renal. Physiol.*, 2002, **282**(2), F179–F190, DOI: 10.1152/ajprenal.2002.282.2.F179 From NLM Medline J. P. Lim and P. A. Gleeson, Macropinocytosis: an endocytic pathway for internalising large gulps, *Immunol. Cell. Biol.*, 2011, **89**(8), 836–843, DOI: 10.1038/icb.2011.20 From NLM Medline.

31 M. Balu, G. Lentsch, D. Z. Korta, K. Konig, K. M. Kelly, B. J. Tromberg and C. B. Zachary, In vivo multiphoton-microscopy of picosecond-laser-induced optical breakdown in human skin, *Lasers Surg. Med.*, 2017, **49**(6), 555–562, DOI: 10.1002/lsm.22655 From NLM Medline P. Das, S. Ganguly, S. Margel and A. Gedanken, Immobilization of Heteroatom-Doped Carbon Dots onto Nonpolar Plastics for Antifogging, Antioxidant, and Food Monitoring Applications, *Langmuir*, 2021, **37**(11), 3508–3520, DOI: 10.1021/acs.langmuir.1c00471 From NLM Medline.

32 B. Gawronska-Kozak, Scarless skin wound healing in FOXN1 deficient (nude) mice is associated with distinctive matrix metalloproteinase expression, *Matrix Biol.*, 2011, **30**(4), 290–300, DOI: 10.1016/j.matbio.2011.04.004 From NLM Medline.

33 E. L. McGown, T. van Ravenswaay and C. R. Dumlao, Histologic changes in nude mouse skin and human skin xenografts following exposure to sulfhydryl reagents: arsenicals, *Toxicol. Pathol.*, 1987, **15**(2), 149–156, DOI: 10.1177/019262338701500204 From NLM Medline.

34 V. W. Wong, M. Sorkin, J. P. Glotzbach, M. T. Longaker and G. C. Gurtner, Surgical approaches to create murine models of human wound healing, *J. Biomed. Biotechnol.*, 2011, **2011**, 969618, DOI: 10.1155/2011/969618 From NLM Medline.

35 M. Wang, J. Zhang, C. Qiao, S. Yan and G. Wu, Comparative analysis of human and mouse transcriptomes during skin wound healing, *Front Cell. Dev. Biol.*, 2024, **12**, 1486493, DOI: 10.3389/fcell.2024.1486493 From NLM PubMed-not-MEDLINE.

36 A. Barbul, T. Shawe, S. M. Rotter, J. E. Efron, H. L. Wasserkrug and S. B. Badawy, Wound healing in nude mice: a study on the regulatory role of lymphocytes in fibroplasia, *Surgery*, 1989, **105**(6), 764–769. From NLM Medline.

37 T. E. Meyerrose, P. Herrbrich, D. A. Hess and J. A. Nolta, Immune-deficient mouse models for analysis of human stem cells, *Biotechniques*, 2003, **35**(6), 1262–1272, DOI: 10.2144/03356ss06 From NLM Medline J. S. Park and K. H. Park, Light enhanced bone regeneration in an athymic nude mouse implanted with mesenchymal stem cells embedded in PLGA microspheres, *Biomater. Res.*, 2016, **20**, 4, DOI: 10.1186/s40824-016-0051-9 From NLM PubMed-not-MEDLINE G. Adigbli, S. Menoret, A. R. Cross, J. Hester, F. Issa and I. Anegon, Humanization of Immunodeficient Animals for the Modeling of Transplantation, Graft Versus Host Disease, and Regenerative Medicine, *Transplantation*, 2020, **104**(11), 2290–2306, DOI: 10.1097/TP.0000000000003177 From NLM Medline.

38 J. B. Johnson, D. A. Broszczak, J. S. Mani, J. Anesi and M. Naiker, A cut above the rest: oxidative stress in chronic wounds and the potential role of polyphenols as therapeutics, *J. Pharm. Pharmacol.*, 2022, **74**(4), 485–502, DOI: 10.1093/jpp/rgab038 From NLM Medline.

39 C. Fruijtier-Pölloth, Safety assessment on polyethylene glycols (PEGs) and their derivatives as used in cosmetic products, *Toxicology*, 2005, **214**(1), 1–38, DOI: 10.1016/j.tox.2005.06.001; K. Knop, R. Hoogenboom, D. Fischer and U. S. Schubert, Poly(ethylene glycol) in Drug Delivery: Pros and Cons as Well as Potential Alternatives, *Angew. Chem., Int. Ed.*, 2010, **49**(36), 6288–6308, DOI: 10.1002/anie.200902672.

40 Y.-H. Huang, P.-Y. Wu, K.-C. Wen, C.-Y. Lin and H.-M. Chiang, Protective effects and mechanisms of Terminalia catappa L. methenolic extract on hydrogen-peroxide-induced oxidative stress in human skin fibroblasts, *BMC Complementary Altern. Med.*, 2018, **18**(1), 266, DOI: 10.1186/s12906-018-2308-4.

41 B. C. Carney, C. M. Simbulan-Rosenthal, D. S. Rosenthal and J. W. Shupp, A Nude Mouse Model of Xenografted Hypertrophic Scar Cells to Test Therapeutics in the Skin, *Front Biosci.*, 2024, **29**(6), 230 From NLM Medline S. M. Alrobaiea, J. Ding, Z. Ma and E. E. Tredget, A Novel

Nude Mouse Model of Hypertrophic Scarring Using Scratched Full Thickness Human Skin Grafts, *Adv. Wound Care*, 2016, **5**(7), 299–313, DOI: **10.1089/wound.2015.0670** From NLM PubMed-not-MEDLINE.

42 P. Zawodny, N. Wahidi, P. Zawodny, E. Duchnik, E. Stoj, W. R. Malec, M. Kulaszynska, K. Skonieczna-Zydecka and J. Sienko, Evaluation of the Efficacy of the 755 nm Picosecond Laser in Eliminating Pigmented Skin Lesions after a Single Treatment Based on Photographic Analysis with Polarised Light, *J. Clin. Med.*, 2024, **13**(2), 304, DOI: **10.3390/jcm13020304** From NLM PubMed-not-MEDLINE.

43 Y.-J. Wang, C.-C. Chang, M.-E. Lu, Y.-H. Wu, J.-W. Shen, H.-M. Chiang and B.-S. Lin, Photoaging and Sequential Function Reversal with Cellular-Resolution Optical Coherence Tomography in a Nude Mice Model, *Int. J. Mol. Sci.*, 2022, **23**(13), 7009.

44 S. Saha, D. Müller and A. G. Clark, Mechanosensory feedback loops during chronic inflammation, *Front. Cell. Dev. Biol.*, 2023, **11**, 1225677.

45 T. Liu, L. Zhang, D. Joo and S.-C. Sun, NF-κB signaling in inflammation, *Signal Transduction Targeted Ther.*, 2017, **2**(1), 17023, DOI: **10.1038/sigtrans.2017.23**; R. Zhong, L. Miao, H. Zhang, L. Tan, Y. Zhao, Y. Tu, M. Angel Prieto, J. Simal-Gandara, L. Chen and C. He, *et al.*, Anti-inflammatory activity of flavonols via inhibiting MAPK and NF-κB signaling pathways in RAW264.7 macrophages, *Curr. Res. Food Sci.*, 2022, **5**, 1176–1184, DOI: **10.1016/j.crfs.2022.07.007**.

46 D. Chen, G. Tan, S. Tian, L. Han, Y. Li, Y. Tan and K. Chen, Advancements in nanozymes research for the management of chronic wounds, *Chem. Eng. J.*, 2024, **500**, 157299, DOI: **10.1016/j.cej.2024.157299**.